Computers & Geosciences 152 (2021) 104738

Contents lists available at ScienceDirect

Computers and Geosciences

journal homepage: www.elsevier.com/locate/cageo

Case study

Empirical subspace detection applied to triggered seismicity by the July 25, 2011, M_w 5.0 earthquake in the Sea of Marmara, Turkey

Camilo De La Hoz [a], Jean Baptiste Tary [a,*], Anthony Lomax [b]

[a] Departamento de Geociencias, Universidad de los Andes, Bogotá, Colombia
[b] ALomax Scientific, 320 Chemin des Indes, 06370, Mouans Sartoux, France

ARTICLE INFO

Keywords:
Data processing
Seismology
Clustering
Statistical methods
Subspace detection

ABSTRACT

The northern branch of the North Anatolian Fault in the Sea of Marmara (SoM) shows a complex seismological behavior including shallow, fluid-related seismicity, deep seismicity, and locked and creeping segments. On July 25, 2011, a M_w 5 earthquakes occurred at a depth of ~ 11.5 km in the western SoM and immediately followed by hundreds of triggered micro-earthquakes mostly outside the rupture area of the mainshock. We here present the application of empirical subspace detector to improve the detection of small events belonging to this sequence and compare these results with the match-filter technique. Using first the station with the highest signal-to-noise ratio, three main clusters are obtained with one cluster of 27 events and two clusters of 3 events leading to 1056 child-events detected. The child-events were manually selected and picked, and 457 child-events were located with NonLinLoc. The empirical subspace detector leads then to ~ 5.5 times more events located compared with the number of parent events, and ~ 1.6 times more events located than the match-filter technique. The subspace detector technique is sensitive mostly to the frequency band for filtering and the clustering parameters. Small changes in these parameters can lead to significantly different detection results. Extending the subspace detector to include network subspace statistics instead of a single station allows the inclusion of different stations and components, and should decrease the important false detection rate observed. The application of the empirical subspace detector to this sequence confirms the potential of this technique to improve event detection and better define spatio-temporal seismicity patterns.

1. Introduction

Automatic earthquake detection is a long-standing issue due to the presence of both random and coherent noises contaminating seismological data. Different methods addressing this issue have been developed over the years, including routine algorithms such as the STA/LTA (short-term average/long-term average) (e.g., Romero et al. (2016)), algorithms based on autoregressive models and Akaike Information Criterion (e.g., Sleeman and van Eck (1999)), advanced data filtering (Botella et al., 2003), and more recently the developments of schemes based on machine learning and convolutional neural networks (e.g., Perol et al. (2018); Mousavi et al. (2020); Wilkins et al. (2020); Wiszniowski et al. (2021)). These algorithms can detect earthquakes with a wide variety of waveforms.

Other methods based on waveform similarity, particularly appropriate for earthquake sequences containing event clusters, find events that are not picked by standard detection methods such as the STA/LTA because of their low signal-to-noise ratios (SNR). The obtained similar events are smaller events located close to the original events having only slightly different source and propagation path. A widely used method called match-filter is based on the similarity between parent events with high SNR with other events, called child-events, with low SNR buried within the continuous time series (e.g., Gibbons and Ringdal (2006); Brown et al. (2008); Mu et al. (2017)). Event similarity measures based on waveforms across the complete network are especially well-suited for event detection (Brown et al., 2008). Using detection methods based on template matching lead to a large increase in the number of events detected, especially for event clusters.

Contrary to the match-filter method, subspace detection first builds a base of singular vectors ("signal vectors") using events from the same cluster to represent the information contained by the original events (Harris, 2006). Using these singular vectors instead of template events, the subspace detection method introduces more variability within the waveforms employed for detection and can lead to the detection of more

* Corresponding author.
E-mail address: jb.tary@uniandes.edu.co (J.B. Tary).

https://doi.org/10.1016/j.cageo.2021.104738
Received 26 May 2020; Received in revised form 18 February 2021; Accepted 24 February 2021
Available online 7 April 2021

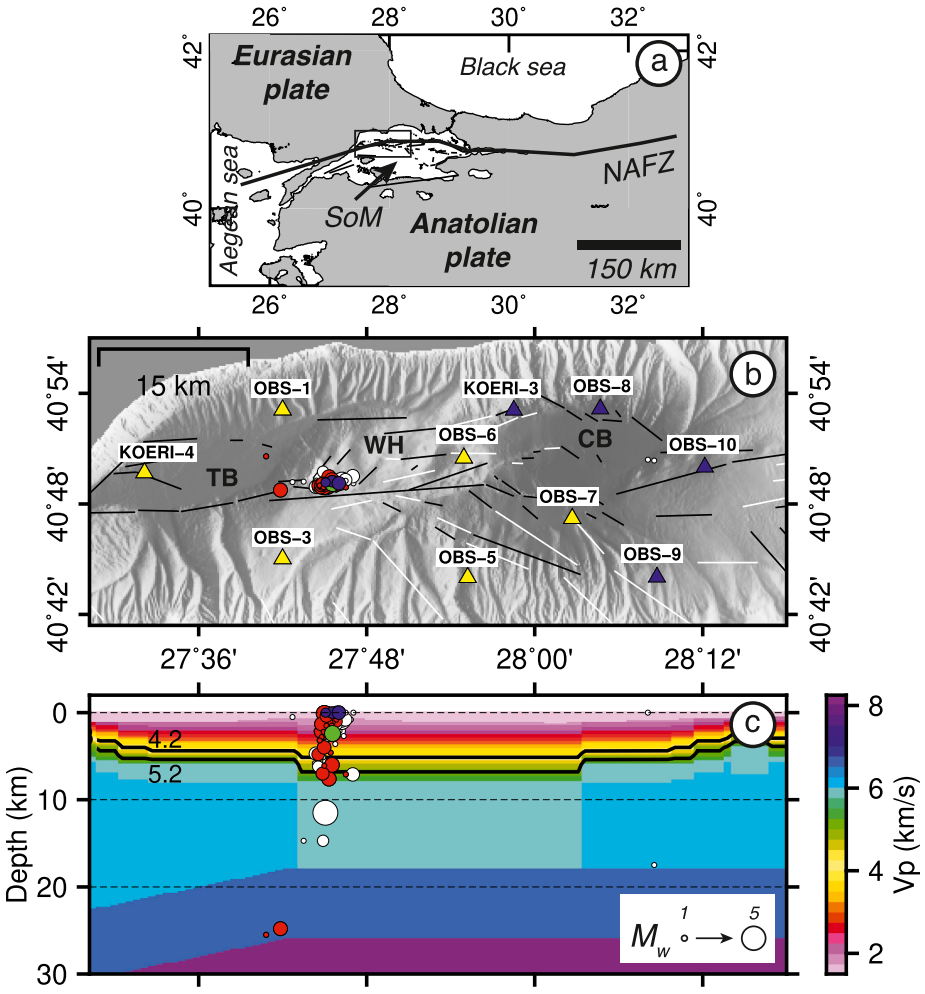

Fig. 1. a) Location of the SoM and the North Anatolian Fault zone (NAFZ). The position of the map in b) is shown by the black rectangle. b) Positions of the OBS deployed in 2011 in the western part of the SoM (triangles). The OBS used for subspace detection processing are indicated by yellow triangles. Active and supposedly inactive faults are indicated by white and black lines, respectively (Şengör et al., 2014). c) East-West cross-section through the 3D velocity model of Géli et al. (Géli et al., 2018) at latitude N40°48'. In both b) and c), parent events are indicated by circles scaling with their magnitudes. Red, green and blue circles are parent events corresponding to cluster 1, 2 and 3, respectively. Abbreviations: TB (Tekirdağ basin), WH (Western High), CB (Central basin). (For interpretation of the references to colour in this figure legend, the reader is referred to the Web version of this article.)

events than the match-filter. Since its introduction by Harris (2006), the subspace detection method has been applied in different contexts (Maceira et al., 2010; Song et al., 2014; Chambers et al., 2015; Socheleau et al., 2015; McMahon et al., 2017; Bestmann and van der Baan, 2017; Morton et al., 2018). The empirical subspace detection technique is a variant of the subspace detection using the event stack and its derivatives for detection instead of singular vectors.

In the present study we focus on a case study comparing the match filter with the application of the empirical subspace detection technique to the mainshock-triggered events sequence containing a M_w 5 earthquake from July 25, 2011, in the Sea of Marmara (SoM). The SoM is located in the western part of the North Anatolian fault (NAF) (Fig. 1). The northern branch of the NAF in the SoM, passing approximately 15 km south of the city of Istanbul, forms a seismic gap capable of generating an earthquake of magnitude ~ 7–8 (Lange et al., 2019). Since the last two large earthquakes in 1999 that happened at the eastern end of the SoM, many studies have been carried out to better define the seismological behavior of the NAF in the SoM (e.g., Bohnhoff et al. (2013); Schmittbuhl et al. (2016a); Lange et al. (2019)).

The NAF in the SoM is characterized by high seismic activity but this activity is not evenly distributed. Intense seismic activity is located mostly within the Çinarcik, Central and Tekirdağ basins and the Western High (Tary et al., 2011; Karabulut et al., 2011; Yamamoto et al., 2015, 2017; Schmittbuhl et al., 2016a; Batsi et al., 2018). Zones exhibiting high seismic activity were generally associated with creeping, or partially creeping segments (Yamamoto et al., 2019), while zones showing low seismic activity were associated with locked segments (Schmittbuhl et al., 2016a; Lange et al., 2019). Seismic repeaters, constituting another potential indicator of creeping behavior, are also observed in different areas of the NAF in the SoM such as the Western High (Schmittbuhl et al., 2016b; Bohnhoff et al., 2017).

The M_w 5 event from July 25, 2011, is one of the highest magnitude earthquake that recently occurred in the western SoM (Pinar et al., 2016), together with the M_w 5.8 Silivri earthquake sequence in September 2019 (Karabulut et al., 2021). The earthquake from July 25, 2011, located at ~ 11.5 km below the Western High (Fig. 1), was almost immediately followed by few hundreds of shallow events (<5 km) (Géli et al., 2018). These events are located approximately 5–10 km away from the mainshock hypocenter, well outside the mainshock rupture area, and are hence considered as triggered seismicity and not aftershocks. The position and immediate triggering of this sequence could be explained by the combined effects of dynamic stresses and local pore pressure increases (Tary et al., 2019).

We employ 85 parent events with high SNR, including shallow and deep events, to design the empirical subspace detector. The child-events detected with the empirical subspace technique are manually selected and picked, and then located with NonLinLoc (Lomax et al., 2001, 2009) using a 3D velocity model (Géli et al., 2018). We then compare the results of the original detections, the match-filter detections (Tary et al., 2019) with those obtained with the empirical subspace technique. We finally discuss the possibility to include all stations of the network within the empirical subspace detector, and the influence of the main parameters on the results.

2. Dataset

Ten autonomous Ocean Bottom Seismometers (OBS) from IFREMER (Institut Français de Recherche pour l'Exploitation de la Mer) were deployed from April 15, 2011, to July 31, 2011, mostly in the central and western SoM (Fig. 1). One of the OBS (OBS-2), that was located on the Western high above the earthquake sequence, stopped functioning on July 1, 2011. In this area, the network is complemented by two permanent seafloor observatories from KOERI (Kandilli Observatory and Earthquake Research Institute). The OBS have a 3-C short-period geophone (Geospace GS-11D, natural frequency of 4.5 Hz) and a hydrophone with a sampling frequency of 125 Hz. The permanent seafloor observatories have a 3-C broad-band seismometer (Guralp CMG-3T) and a hydrophone with a sampling frequency of 100 Hz.

In this study we focus on the data from a sub-network centered on the Western High that consists of five OBS (OBS-1, 3, 5, 6 and 7) and one seafloor observatory (KOERI-4). This selection is based on the data quality of the time picks done for the original dataset (Géli et al., 2018). The zone of the NAF in the Western High is characterized by shallow and deep seismicity (Schmittbuhl et al., 2016a; Géli et al., 2018), and by important fluid activity with different expressions such as gas bubbles in the water column (Dupré et al., 2015), free-gas accumulations and gas hydrates (Thomas et al., 2012), and important mud bodies in the superficial sediments (Grall et al., 2013).

3. Methods

3.1. Match-filter and subspace detection

Starting with 85 parent-events (Fig. 1), the match-filter was applied to continuous time series from April 15, 2011, to July 31, 2011, filtered between 15 and 25 Hz. Cross-correlations between parent events and the time series were performed separately for each OBS, then re-aligned using parent event moveout, summed, and a detection was declared if a median absolute deviation (MAD) threshold of 10 is reached with at least three cross-correlation coefficients greater than 0.65. Pick timings can be calculated automatically using cross-correlation (Tary et al., 2019). In the present case we select and pick manually the events in order to follow the same procedure as for the subspace detection method. Child-events are then located with NonLinLoc and a 3-D velocity model of the SoM (Bayrakci et al., 2013; Géli et al., 2018). Using this match-filter approach, 1266 events were detected, 455 events were selected and picked (i.e., 811 events were false detections), and 365 child-events with at least 6 phase picks were finally located. Out of these 365 events, 88 occurred before and 277 after the mainshock. Performing the selection and picking mostly manually, instead of automatically as in (Tary et al., 2019), increased more than two-fold the final number of events located.

As with the match-filter, the subspace detection method classifies a signal window taken from continuous data as either signal plus noise or noise (Maceira et al., 2010). For the subspace method, the continuous data is assumed to be a combination of orthonormal signal vectors **U** and a set of weights. The set of orthonormal vectors is first determined through the singular value decomposition (SVD) of a matrix of parent events **A** previously classified in clusters as,

$$\mathrm{SVD}(\mathbf{A}) = \mathbf{U}\mathbf{S}\mathbf{V}^{\mathrm{T}}, \tag{1}$$

where **U** is a matrix of left-singular vectors used for detection, **S** is a matrix containing the singular values, and **V** is a matrix of right-singular vectors. The similarity metric for detection corresponds to the projection of the continuous data d on a subset of singular vectors $\mathbf{U}_s$ coming from matrix **U** as,

$$z = \frac{d^{\mathrm{T}}\mathbf{U}_s\mathbf{U}_s^{\mathrm{T}}d}{d^{\mathrm{T}}d}. \tag{2}$$

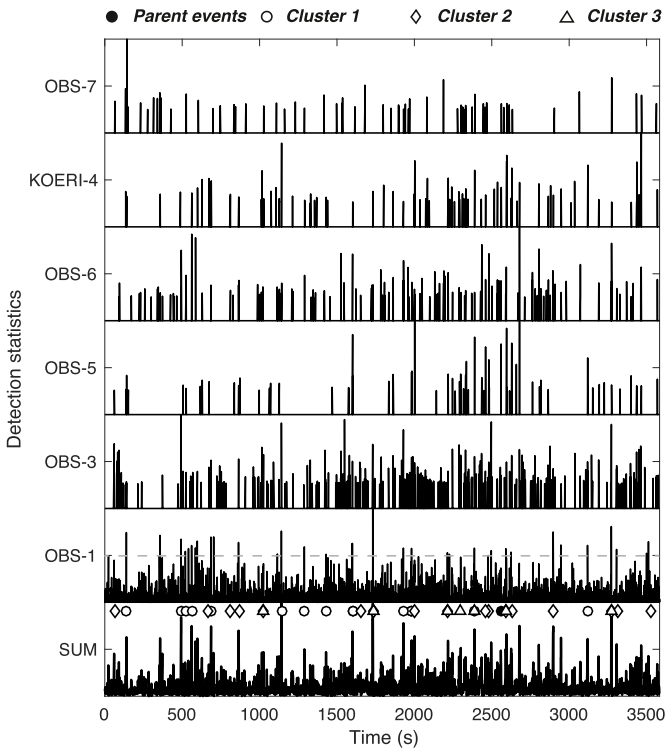

Fig. 2. Detection statistics using equation (2) (1 hour on 26/07/2011 starting at 0am) for cluster 1 and the selected stations of the network, as well as the sum of station detection statistics calculated using equation (3). The gray dashed line indicates the detection threshold of 0.5 for OBS-1. Timings of parent events (black dots) and child-events for each cluster are also indicated by white dots (cluster 1), white diamonds (cluster 2) and white triangles (cluster 3).

In the present study we use the empirical subspace detection technique (Barrett and Beroza, 2014) instead of the subspace detection method (Harris, 2006) due to its higher detection potential. In this case, the matrix $\mathbf{U}_s$ is made of the stack and its first derivative relative to time which are sometimes highly similar to the first and second singular vectors, respectively, of the standard subspace method. The empirical subspace detector is applied using a single component of a station (OBS-1, vertical component), using the complete event waveforms including P- and S-waves, and with data band-pass filtered between 5 and 15 Hz. For clustering, we use the single-linkage algorithm based on the Euclidean distance between events and a cross-correlation coefficient threshold of 0.8 to determine links between events. A conservative detection threshold on z was determined by trial-and-error and set to 0.5 (Fig. 2). In order to include the geophone's 3 components, we tested multiplexing parent-event waveforms and continuous data before detection but this did not yield better detection than using a single component. The number of true and false detections both decrease due to multiplexing because this process increases the template singularity which makes the detector more specific. Automatic picking with the singular vectors or the stack was also tested but due to significant differences between singular vectors and detected signals, this picking is not precise enough to obtain reliable earthquake locations. We then picked manually the events detected.

3.2. Potential use of network subspace detection

The original method uses data from a single station and one component to compute detection statistics following equations (1) and (2) (Harris, 2006; Barrett and Beroza, 2014). Detection statistics based on single stations generally lead to many false detections due to impulsive noises present in the data, even though this is less a problem

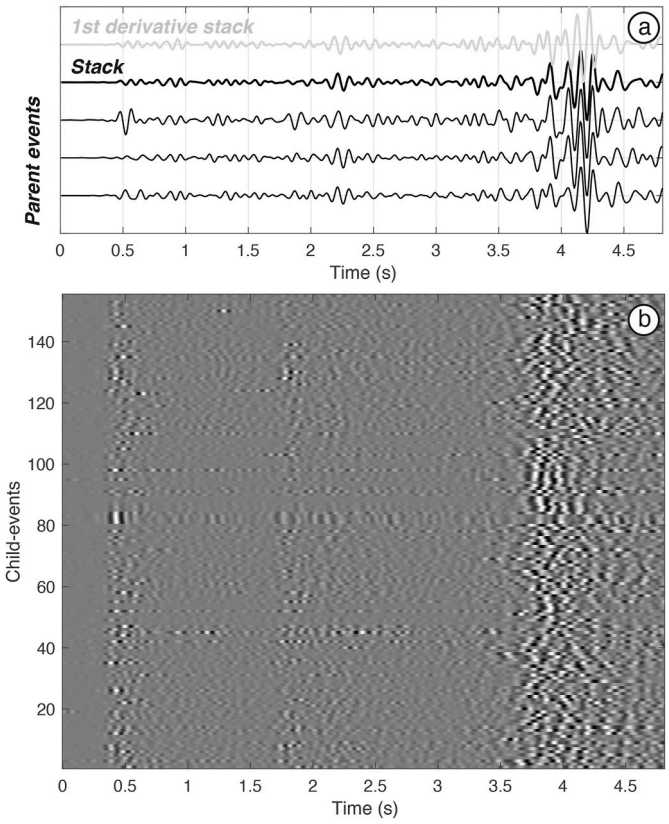

Fig. 3. a) Waveforms (OBS-1, vertical component) corresponding to the 3 parent-events belonging to cluster 2 (thin black lines), and the event stack (thick black line) and 1st stack derivative (gray line) used for the empirical subspace detection. b) Selected child-events (155) obtained with the empirical subspace detector. All waveforms are aligned on their P-wave arrivals (∼ 0.3 sec.) and band-pass filtered between 5 and 15 Hz.

using template matching methods. Combining these statistics for different stations of the network should emphasize coherent events throughout the network and decrease the amount of false detections.

We extend the subspace detection method to include all stations of the network using the following steps. The station as well as the component with the best SNR, OBS-1 and its vertical component in this case, are used as a reference to cluster the events. Events belonging to a specific cluster, selecting only those that have cross-correlation coefficients greater than 0.8, are used in the singular value decomposition and to compute the stack for each OBS. Detection statistics using equation (2) are then calculated for each OBS and finally summed after delaying each time series (e.g., by an average or median moveout calculated over all events belonging to the cluster) using,

$$z_s(t_s) = \sum_{i=1}^{n} w_i z_i(t_i), \tag{3}$$

where n is the number of stations, t_i is the specific timing for station i after taking into account event moveouts, and t_s the summation timing (Fig. 2). Each detection statistic can be individually weighted (w_i) to take into account different data quality.

4. Results

4.1. Single station event detections

Using 85 parent events and the parameters described in the previous sections, we obtain 3 main clusters with 3 or more events. All 3 clusters belong to the superficial seismicity mainly located between 0 and 5 km depths. The first cluster contains 27 events, and clusters 2 (Fig. 3) and 3 contain 3 events (see Fig. 1 for cluster locations). From a total number of detections of ∼ 16900 and after removing false detections and duplicates, 1056 events were identified including 426, 408 and 222 events for cluster 1, 2, and 3, respectively. We then selected events with at least 6 phase picks for location leading to 180, 155 and 122 events for cluster 1, 2, and 3, respectively (Fig. 4).

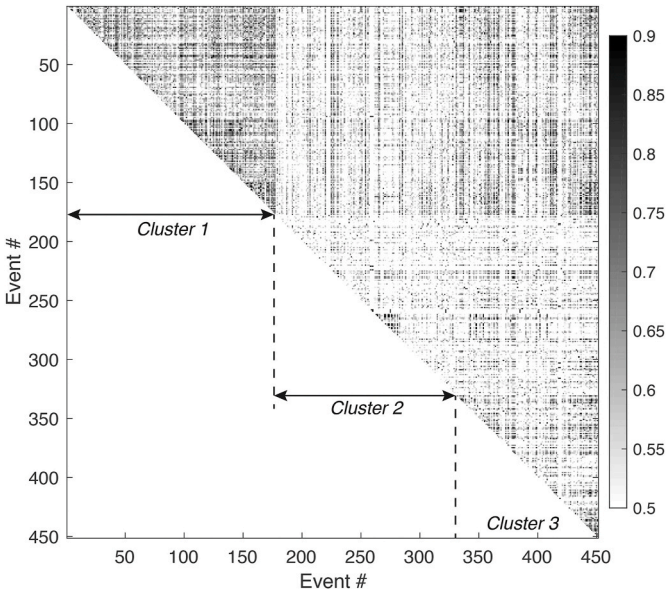

Fig. 4. Full waveform cross-correlation coefficients between child-events detected with the empirical subspace detector (OBS-1, vertical component, signals filtered between 5 and 15 Hz).

4.2. Network empirical subspace

In the present case, waveforms from OBS vertical components and the same frequency band (5–15 Hz) were employed to build the cross-correlation matrix and cluster the events for all OBSs. Detection statistics obtained for each OBS are not summed using a specific moveout but in a sliding window of 2 sec to take into account potential different moveouts. Each $z-$ statistic time series is first normalized by their maximum amplitude, then re-weighted and finally summed altogether. Only OBS-1 $z-$ statistic has a higher weight of 2, and $z-$ statistics of OBSs 5 and 7 are not included due to their lower data quality (Fig. 5). Any z value lower than 0.25 is set to 0 in order to avoid contaminating the sum.

Fig. 5a and b shows the case of a an event seen at different OBSs and presenting a high summed z_s value. While many events detected using the single station empirical subspace detector are also detected using the z_s statistic (up to 100% of the events for some hours), many are left out due to the specificity of the current dataset. In some instances, the stack and first stack derivative used for detection are significantly different from some event waveforms at some stations only. This leads to lower z_s values and difficulties to detect those events (Fig. 5c and d). Here, data quality is much higher for one station in particular (OBS-1), decreasing the advantage of using network statistics for detection. The empirical subspace method using network statistics would be indicated for denser networks.

4.3. Event locations

Locations obtained with NonLinLoc of parent and child-events using the match-filter and the subspace detector are shown in Fig. 6. In the present case, there exists for many events an ambiguity between shallow (0–5 km) and deep locations (10–30 km) with probability density

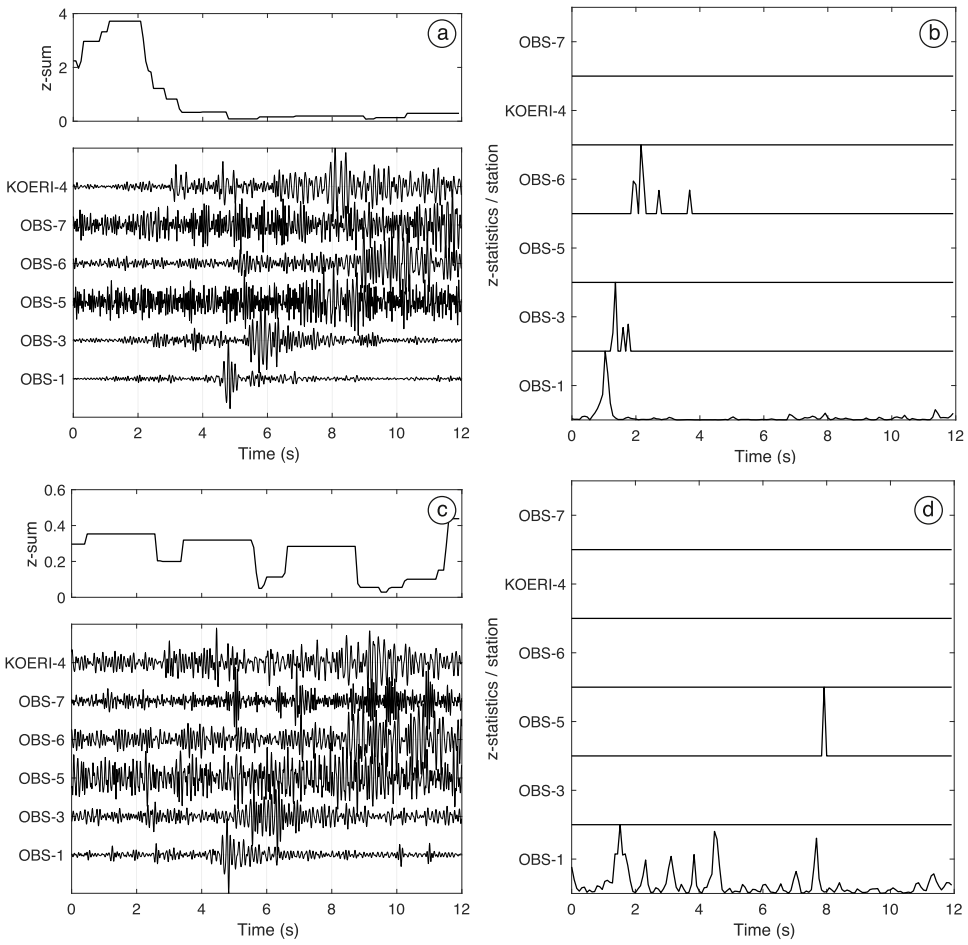

Fig. 5. Examples of waveforms and *z* statistics for two micro-earthquakes (a) and b): 26/07/2011 00:08:10; c) and d): 26/07/2011 01:52:15). All waveforms are OBSs vertical components and band-pass filtered between 5 and 15 Hz.

functions having two maxima. This is due to the presence of localized, low velocity layers in the first few km and the lack of a station above the seismicity. This also explains the inclusion of two deep events in cluster 1 (Fig. 1). Tests carried out using the parent events (Géli et al., 2018) and comparisons between deep (i.e., the mainshock) and shallow parent events (Tary et al., 2019) indicate that shallow locations are more likely. Child- and parent-events generally have high cross-correlation coefficients and similar travel-times showing that they share the same source area. We then restricted the location procedure to positions above 10 km in NonLinLoc in order to avoid the shallow-deep ambiguity. These are the locations shown in Fig. 6c.

5. Discussion

5.1. Empirical subspace detections

The first event detected after the mainshock (25/07/2011 18:03:16) by the empirical subspace detector and located in the shallow cluster (depth of 1.6 km) occurs less than 6 min after the mainshock. Since most of the child-events are highly correlated to parent events located in the shallow cluster, these events are likely located in this cluster as well. The total number of detections for the match-filter is approximately three-times lower than for the empirical subspace detector (327 and 1056, respectively) considering the same time period. The apparently low number of detections for both techniques is due to the low number of stations able to record the events. Moreover, for the subspace detector, the setup using a single station for detection and the similarity between moveouts due to the high seismicity concentration in this area for this time period limits the waveform variability and is impacting more the subspace detector than the match-filter. Despite this limitation, the numbers of selected and located events (277 for the match-filter and 457 for the empirical subspace detector) are higher for the subspace detection method. This arises partly due to the larger waveform variability included in the subspace detection method, and possibly also due to differences in each method settings leading to different expected false alarm rate (Song et al., 2014).

We introduce one possible way to extend the subspace method to include all stations of the network. Using network statistics should allow to both detect a larger variety of events including a larger variety of moveouts and SNR, and avoid a number of false alarms by combining information at different stations. In the present case, the network subspace detector is setup using a time window to search for different moveouts, but other schemes are possible such as, for example, the use of average moveouts of events from know clusters. In a similar way, one could include all 3 components of each station as well. Having different detection statistics for each station and component leaves the possibility to combine then in different ways to maximize event detection.

One of the most important steps for the subspace detection technique is the selection and clustering of parent events. The clustering based on complete waveforms as well as the detection are mainly controlled by arrivals with higher SNR (high amplitude conversions and S-waves in our case). The clustering step is in turn impacted by the frequency band used and the threshold set on the cross-correlation coefficients to link events. For example in our case, changing the frequency band from 5 -

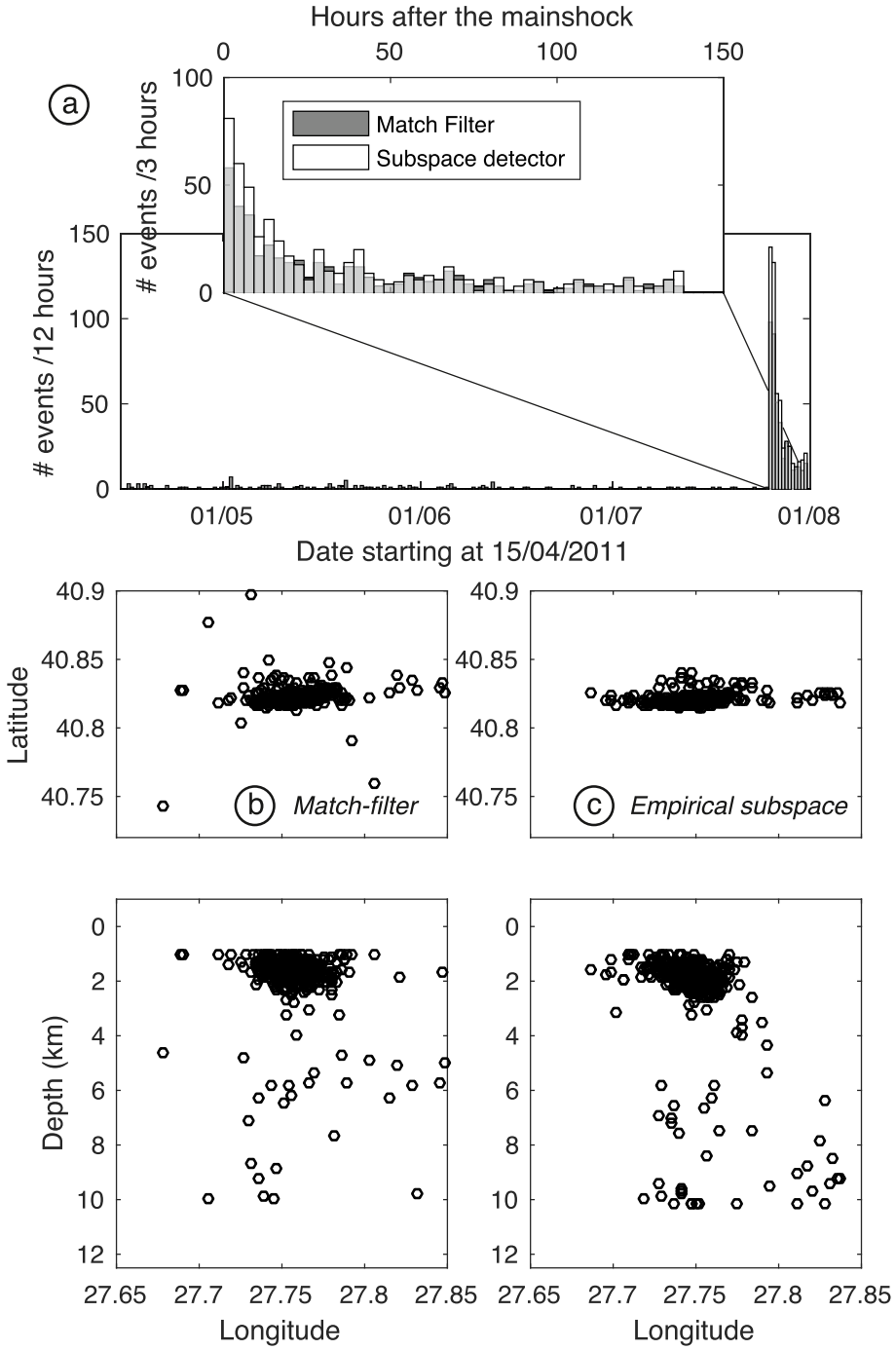

Fig. 6. a) Temporal evolution before and after the mainshock of the number of events detected with the match-filter and the empirical subspace detector. Locations, constrained to less than 10 km depth, obtained for the child-events detected with the match-filter in b) and the empirical subspace detector in c), showing events with more than 6 phase picks and uncertainties lower than 10 km.

15 Hz to 5–20 Hz changes the number of events in cluster 1 from 27 to 11, and then might change which events belongs to other clusters. This effect is due to the template events becoming more singular (i.e., owing to noisier and more complex signals) when one use wider frequency bands, decreasing their possible similarity with other events or continuous time series. These parameters may be chosen by reviewing the clustering results using different parameter sets (e.g., presence of noisy traces, high similarity of waveforms in clusters, high number of events in clusters). In the present study, we determine these parameters using the station with the best SNR and then use the parameters corresponding to these clustering results to carry out the SVD or the stack on the other stations of the network. If a number of stations have similar SNR, one could combine the clustering information from these stations to define the final set of events to include in the clusters. Which events to include in the SVD/stack at other stations could also be refined using an additional clustering step based on their cross-correlation coefficients for each station.

Table 1
Dynamic stress variation computing parameters.

Mainshock focal mechanism[a]	strike 113, dip 83, rake −148
Superficial event focal mechanism[a]	strike 300, dip 34, rake −143
Friction coefficient μ[b]	0.25
Skempton coefficient B[c]	0.6
S-wave velocity β	3000 m/s
Rigidity modulus G	30 GPa
Rise times τ[d]	0.07 s (M_w 3), 0.14 s (M_w 4), 0.3 s (M_w 5)

[a]Batsi et al. (Batsi et al., 2018)
[b] for clay-rich faults (Remitti et al., 2015)
[c] case of water-saturated rocks
[d] calculated using scaling relationships (Geller, 1976)

5.2. Event sequence interpretation

Both the match-filter and empirical subspace detection processes confirm the important increase in microseismicity just after the M_w 5 mainshock (25/07/2011 17:57:34). The sequence is taking place below the Western High in a partially creeping section of the NAF (Yamamoto et al., 2019). Background seismicity in this zone is also characterized by an elongated cluster going from deep (∼ 15–17 km) to shallow levels (∼ 0–5 km) (Schmittbuhl et al., 2016a). Moderate size events (i.e., 4 < M_w <6) occurring at different depth levels in the SoM lead to static stress variations only in their vicinity, and important dynamic stresses in the sedimentary basins. To evaluate a potential influence of deep events of different magnitudes on the different depth levels, we compute dynamic Coulomb stress variations $\Delta\sigma_c$ due to the mainshock with (Beeler et al., 2000),

$$\Delta\sigma_c = \Delta\tau - \mu(\Delta\sigma_n + \Delta P), \quad (4)$$

where $\Delta\tau$ is the shear stress variation in the slip direction calculated on the receiver fault plane, $\Delta\sigma_n$ is the normal stress variation, μ is the friction coefficient, and ΔP is the pore pressure variation given by $\Delta P = -B\frac{\Delta\sigma_{kk}}{3}$ (with B the Skempton coefficient, and $\Delta\sigma_{kk}/3$ the mean stress variation). Dynamic stress variations are calculated using AXITRA (Cotton and Coutant, 1997), which employ the reflectivity method (Kenneth and Kerry, 1979) with the discrete wavenumber method (Bouchon, 1981), a 1D velocity model extracted from the 3D velocity model of Géli et al. (2018), and receiver fault parameters corresponding to the composite focal mechanism of the superficial events (Batsi et al., 2018). Computations parameters are summarized in Table 1. Fig. 7a shows that significant dynamic stress variations, between ∼ 300 kPa and ∼ 35 kPa in absolute value, are present at all depths. Events with magnitudes between M_w4 and 5 generate dynamic stresses between ∼ 5 and ∼ 35 kPa in shallow sediments.

The additional events detected by the match-filter before the mainshock are mostly located at the approximate position of the superficial cluster, with very few events located at depth. As shown by Schmittbuhl et al. (2016a) as well, the shallow part of the Western High presents then a sustained seismic activity. Dynamic stress variations of the order of few tens of kPa or more, together with high pore pressures in this area, could then promote the seismicity in this region. The cause of the July 2011 triggered event sequence, could then involve an interplay of few factors including a deep-shallow connection for seismicity and fluids (Géli et al., 2018), in addition to fault and stress complexity (Schmittbuhl et al., 2016a), and dynamic triggering from a moderate size event in levels with high fluid pressures. Similar seismicity promoting conditions of high pore pressures and tectonic activity could be present in other parts of the SoM (e.g., Grall et al. (2018)).

6. Conclusion

We present a comparison of match filter and empirical subspace methods applied to a case study in the SoM including a large event cluster. The empirical subspace method should give a larger number of detections since it keeps more variability in the waveforms used for detection (i.e., singular vectors or the stack and its derivatives). In the present case, 277 and 457 events were located using the match-filter and the empirical subspace detector, respectively, during the same time period. In comparison with the 85 original parent events, this corresponds to a ∼ 5.5-fold increase in the number of events located. We are here limited mainly by the number of stations in the network, limiting the number of phases for location. The subspace detection technique can also be extended to include the 3-components of all stations of the network in order to both include more events and decrease the number of false detections. For the M_w 5.0 July 25, 2011, triggered sequence, dynamic stress perturbations could promote microseismicity in the shallow section of the NAF below the Western High. Improved detection to extract smaller magnitude events from continuous data helps then to better define the spatio-temporal evolution of microseismicity, in turn improving the understanding of its different driving processes.

Data availability

Seismological data from IFREMER used in this study are available at

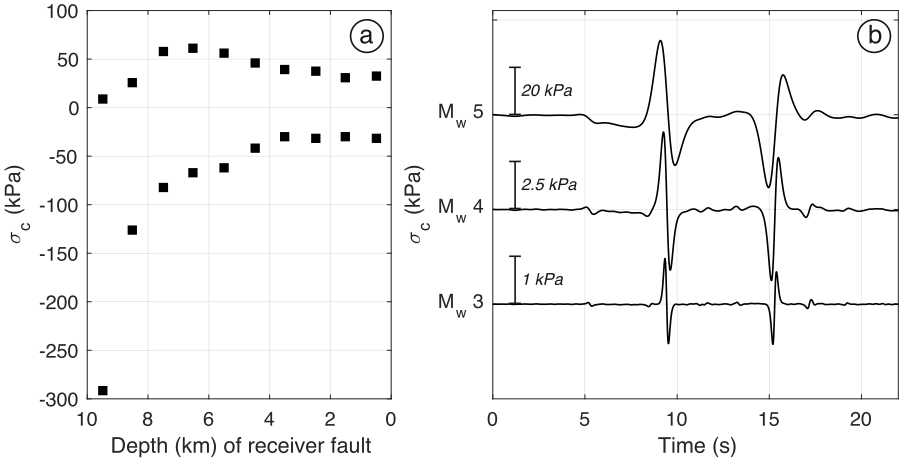

Fig. 7. Dynamic stress calculations of Coulomb stress for a) different receiver fault depths (minimum and maximum stresses in each case), and b) different mainshock magnitudes (mainshock and receiver fault at 11.5 and 1.5 km depth, respectively). The receiver fault corresponds to the composite focal mechanism for the superficial events. See Table 1 for the computing parameters.

SEANOE https://doi.org/10.17882/49764.

Computer code availability

A series of MATLAB codes implementing the technique as well as the parent events and a continuous data example are provided in the following Github repository: https://github.com/EkMuyal/SubspaceDetection. The main codes are named "subspace_marmara_net" and were developed by C. De La Hoz and J. B. Tary from codes provided by G. Beroza. The total code size is 865 MB including parent events and a continuous data example.

Authorship statement

C. De La Hoz and J. B. Tary carried out coding, design and analysis, and wrote the paper, A. Lomax participated in the design and analysis, and revised the paper.

Declaration of competing interest

The authors declare that they have no known competing financial interests or personal relationships that could have appeared to influence the work reported in this paper.

Acknowledgments

The seismological data were acquired within the ESONET Network of Excellence (contract N^o 036851). Jean Baptiste Tary was funded by the FAPA project from the Universidad de los Andes (PR.3.2016.3047). We thank two anonymous reviewers for their valuable comments which improved the quality the present study. The Generic Mapping Tools (GMT) was used for Fig. 1.

References

Barrett, S.A., Beroza, G.C., 2014. An empirical approach to subspace detection. Seismol Res. Lett. 85 (3), 594–600.
Batsi, E., Lomax, A., Tary, J., Klingelhoefer, F., Riboulot, V., Murphy, S., Monna, S., Özel, N., Kalafat, D., Saritas, H., Cifçi, G., Çagatay, N., Gasperini, L., Géli, L., 2018. An alternative view of the microseismicity along the Western Main Marmara Fault, based on a high-resolution study. Bull. Seismol. Soc. Am. 108 (5A), 2650–2674.
Bayrakci, G., Laigle, M., Bécel, A., Hirn, A., Taymaz, T., Yolsal-Çevikbilen, S., team, S., 2013. 3-D sediment-basement tomography of the Northern Marmara trough by a dense OBS network at the nodes of a grid of controlled source profiles along the North Anatolian fault, Geophys. J. Intell. 194 (3), 1335–1357.
Beeler, N.M., Simpson, R.W., Hickman, S.H., Lockner, D.A., 2000. Pore fluid pressure, apparent friction, and Coulomb failure. J. Geophys. Res.: Solid Earth 105 (B11), 25533–25542.
Bestmann, I., van der Baan, M., 2017. A comparision of subspace techniques with matched filtering and STA/LTA for detection of microseismic events: a case study. CSEG Geoconvention, Calgary, Canada.
Bohnhoff, M., Bulut, F., Dresen, G., Malin, P.E., Eken, T., Aktar, M., 2013. An earthquake gap south of Istanbul. Nat. Commun. 4, 1999.
Bohnhoff, M., Wollin, C., Domigall, D., Küperkoch, L., Martìnez-Garzón, P., Kwiatek, G., Dresen, G., Malin, P.E., 2017. Repeating Marmara Sea earthquakes: indication for fault creep. Geophys. J. Int. 210 (1), 332–339.
Botella, F., Rosa-Herranz, J., Giner, J.J., Molina, S., Galiana-Merino, J.J., 2003. A real-time earthquake detector with prefiltering by wavelets. Comput. Geosci. 29, 911–919.
Bouchon, M., 1981. A simple method to calculate Green's functions for elastic layered media. Bull. Seismol. Soc. Am. 71 (4), 959–971.
Brown, J.R., Beroza, G.C., Shelly, D.R., 2008. An autocorrelation method to detect low frequency earthquakes within tremor. Geophys. Res. Lett. 35, L16305.
Chambers, D.J.A., Koper, K.D., Pankow, K.L., McCarter, M.K., 2015. Detecting and characterizing coal mine related seismicity in the Western U.S. using subspace methods. Geophys. J. Int. 203, 1388–1399.
Cotton, F., Coutant, O., 1997. Dynamic stress variations due to shear faults in a plane-layered medium. Geophys. J. Int. 128, 676–688.
Dupré, S., Scalabrin, C., Grall, C., Augustin, J.-M., Henry, P., Şengör, A.M.C., Görür, N., Çağatay, M.N., Géli, L., 2015. Tectonic and sedimentary controls on widespread gas emissions in the Sea of Marmara: results from systematic, shipborne multibeam echo sounder water column imaging. J. Geophys. Res. Solid Earth 120, 2891–2912.
Géli, L., Henry, P., Grall, C., Tary, J.B., Lomax, A., Batsi, E., Cros, E., C, G., Isik, S., Sengör, A., et al., 2018. Gas related seismicity within the Istanbul seismic gap. Sci. Rep. 8, 6819.
Geller, R.J., 1976. Scaling relations for earthquake source parameters and magnitudes. Bull. Seismol. Soc. Am. 66 (5), 1501–1523.
Gibbons, S.J., Ringdal, F., 2006. The detection of low magnitude seismic events using array-based waveform correlation. Geophys. J. Int. 165 (1), 149–166.
Grall, C., Henry, P., Thomas, Y., Westbrook, G.K., Çağatay, M.N., Marsset, B., Saritas, H., Çifçi, G., Géli, L., 2013. Slip rate estimation along the western segment of the Main Marmara Fault over the last 405-490 ka by correlating mass transport deposits. Tectonics 32, 1587–1601.
Grall, C., Henry, P., Dupré, S., Géli, L., Scalabrin, C., Zitter, A.M.C., andSengor, T.A.C., Cagatay, M.N., Cifci, G., 2018. Upward migration of gas in an active tectonic basin: an example from the sea of Marmara. Deep Sea Res. Part II Top. Stud. Oceanogr. 153, 17–35.
Harris, D., 2006. Subspace Detectors: Theory, Lawrence Livermore Natl. Lab. Rep. UCRL-TR-222758. Lawrence Livermore National Laboratory, Livermore, California.
Karabulut, H., Schmittbuhl, J., Özalaybey, S., Lengliné, O., Kömeç-Mutlu, A., Durand, V., Bouchon, M., Daniel, G., Bouin, M.P., 2011. Evolution of the seismicity in the eastern marmara sea a decade before and after the 17 August 1999 Izmit earthquake. Tectonophysics 510 (1–2), 17–27.
Karabulut, H., Güvercin, S.E., Eskiköy, F., Konca, A.O., Ergintav, S., 2021. The moderate size 2019 September M_w 5.8 Silivri earthquake unveils the complexity of the Main Marmara Fault shear zone. Geophys. J. Int. 224, 377–388.
Kenneth, B.L.N., Kerry, N.J., 1979. Seismic waves in a stratified half space. Geophys. J. Roy. Astron. Soc. 57, 557–583.
Lange, D., Kopp, H., Royer, J., et al., 2019. Interseismic strain build-up on the submarine North Anatolian fault offshore Istanbul. Nat. Commun. 10, 3006.
Lomax, A., Zollo, A., Capuano, P., Virieux, J., 2001. Precise, absolute earthquake location under Somma-Vesuvius volcano using a new three-dimensional velocity model. Geophys. J. Int. 146 (2), 313–331.
Lomax, A., Michelini, A., Curtis, A., 2009. Earthquake Location, Direct, Global-Search Methods in, Encyclopedia of Complexity and System Science, vol. 5. Springer, New York, pp. 2449–2473. Part.
Maceira, M., Rowe, C.A., Beroza, G., Anderson, D., 2010. Identification of low-frequency earthquakes in non-volcanic tremor using the subspace detector method. Geophys. Res. Lett. 37, L06303.
McMahon, N.D., Aster, R.C., Yeck, M.L., McNamara, D.E., Benz, H.M., 2017. Spatiotemporal evolution of the 2011 Prague, Oklahoma, aftershock sequence revealed using subspace detection and relocation. Geophys. Res. Lett. 44, 7149–7158.
Morton, E.A., Bilek, S.L., Rowe, C.A., 2018. Newly detected earthquakes in the Cascadia subduction zone linked to seamount subduction and deformed upper plate. Geology 46 (11), 943–946.
Mousavi, S.M., Ellsworth, W.L., Zhu, W., Chuang, L.Y., Beroza, G.C., 2020. Earthquake transformer–an attentive deep-learning model for simultaneous earthquake detection and phase picking. Nat. Commun. 11 (1), 1–12.
Mu, D., Lee, E.-J., Chen, P., 2017. Rapid earthquake detection through GPU-Based template matching. Comput. Geosci. 109, 305–314.
Perol, T., Gharbi, M., Denolle, M., 2018. Convolutional neural network for earthquake detection and location. Sci. Adv. 4 (2), e1700578.
Pinar, A., Coşkun, Z., Mert, A., Kalafat, D., 2016. Frictional strength of North Anatolian fault in eastern Marmara region. Earth Planets Space 68, 62.
Remitti, F., Smith, S.A.F., Mittempergher, S., Gualtieri, A.F., Di Toro, G., 2015. Frictional properties of fault zone gouges from the J-FAST drilling project (Mw 9.0 2011 Tohoku-Oki earthquake). Geophys. Res. Lett. 42, 2691–2699.
Romero, J.E., Titos, M., Bueno, Ángel, Álvarez, I., García, L., Ángel de la Torre, Benítez, M.C., 2016. APASVO: a free software tool for automatic P-phase picking and event detection in seismic traces. Comput. Geosci. 90, 213–220.
Schmittbuhl, J., Karabulut, H., Lengliné, O., Bouchon, M., 2016a. Seismicity distribution and locking depth along the main marmara fault, Turkey. G-cubed 17, 954–965.
Schmittbuhl, J., Karabulut, H., Lenglién, O., Bouchon, M., 2016b. Long-lasting seismic repeaters in the Central basin of the main marmara fault. Geophys. Res. Lett. 43, 9727–9534.
Şengör, A.M.C., Grall, C., Imren, C., Le Pichon, X., Görür, N., Henry, P., Karabulut, H., Siyako, M., 2014. The geometry of the North Anatolian transform fault in the Sea of Marmara and its temporal evolution: implications for the development of intracontinental transform faults. Can. J. Earth Sci. 51 (3), 222–242.
Sleeman, R., van Eck, T., 1999. Robust automatic P-phase picking: an on-line implementation in the analysis of broadband seismogram recordings. Phys. Earth Planet. In. 113 (1), 265–275. ISSN 0031-9201.
Socheleau, F.-X., Leroy, E., Carvallo Pecci, A., Samaran, F., Bonnel, J., Royer, J.-Y., 2015. Automated detection of Antarctic blue whale calls. J. Acoust. Soc. Am. 138 (5), 3105–3117.
Song, F., Warpinski, N.R., Toksöz, M.N., Kuleli, H.S., 2014. Full-waveform based microseismic event detection and signal enhancement: an application of the subspace approach. Geophys. Prospect. 62 (6), 1406–1431.
Tary, J.B., Géli, L., Henry, H., Natalin, B., Gasperini, L., Çomoglu, M., Çagatay, N., Bardainne, T., 2011. Sea bottom observations from the western escarpment of the Sea of Marmara. Bull. Seismol. Soc. Am. 101, 775–791.
Tary, J.B., Géli, L., Lomax, A., Batsi, E., Riboulot, V., Henry, P., 2019. Improved detection and Coulomb stress computations for gas-related, shallow seismicity, in the Western Sea of Marmara. Earth Planet Sci. Lett. 513, 113–123.
Thomas, Y., Marsset, B., Westbrook, G., Grall, C., Géli, L., Henry, P., Cifci, G., Rochat, A., Saritas, H., 2012. Contribution of high-resolution 3D seismic near-seafloor imaging to reservoir-scale studies: application to the active North Anatolian Fault, Sea of Marmara. Near Surf. Geophys. 10 (4), 291–301.

Wilkins, A.H., Strange, A., Duan, Y., Luo, X., 2020. Identifying microseismic events in a mining scenario using a convolutional neural network. Comput. Geosci. 137, 104418. ISSN 0098-3004.
Wiszniowski, J., Plesiewicz, B., Lizurek, G., 2021. Machine learning applied to anthropogenic seismic events detection in Lai Chau reservoir area, Vietnam. Comput. Geosci. 146, 104628. ISSN 0098-3004.
Yamamoto, Y., Takahashi, N., Citak, S., Kalafat, D., Pinar, A., Gurbuz, C., Kaneda, Y., 2015. Offshore seismicity in the western Marmara Sea, Turkey, revealed by ocean bottom observation. Earth Planets Space 67, 147.
Yamamoto, Y., Takahashi, N., Pinar, A., Kalafat, D., Citak, S., Comoglu, M., Polat, R., Kaneda, Y., 2017. Geometry and segmentation of the North Anatolian Fault beneath the Marmara Sea, Turkey, deduced from long-term ocean bottom seismographic observations. J. Geophys. Res. 122, 2069–2084.
Yamamoto, R., Kido, M., Ohta, Y., Takahashi, N., Yamamoto, Y., Pinar, A., et al., 2019. Seafloor geodesy revealed partial creep of the north Anatolian fault submerged in the sea of Marmara. Geophys. Res. Lett. 46, 1268–1275.